Journal of Physical Oceanography

The DOI for this manuscript is doi: 10.1175/2009JPO3985.1

Using transformation and formation maps to study the role of air-sea heat fluxes in North Atlantic Eighteen Degree Water formation.

Guillaume Maze *

Gael Forget

Martha Buckley

John Marshall

Massachusetts Institute of Technology

Ivana Cerovecki

Scripps Institution of Oceanography

January 22, 2009

---

[*] *Corresponding author address:* Guillaume Maze, MIT-EAPS: 54-1424, 77 Massachusetts Av., Cambridge, MA 02139, USA. E-mail: gmaze@mit.edu

Abstract

Walin's (1982) water mass framework quantifies the rate at which water is transformed from one temperature class to another by air-sea heat fluxes (transformation). The divergence of the transformation rate yields the rate at which a given temperature range is created or destroyed by air-sea heat fluxes (formation). Walin's framework provides a precise integral statement at the expense of losing spatial information. In this study we plot out the integrand of Walin's expression to yield transformation and formation maps and use them to study the role of air-sea heat fluxes in the cycle of formation/destruction of the 18 ± 1^oC layer in the North-Atlantic.

Using remotely-sensed sea surface temperatures and air-sea heat flux estimates based on both analyzed meteorological fields and ocean data-model syntheses for the three-year period 2004–2006, we find that EDW is formed by air-sea heat fluxes in the western part of the subtropical gyre, just south of the Gulf Stream. The formation rate peaks in February when the EDW layer is thickened by convection due to buoyancy loss. EDW is destroyed by air-sea heat fluxes from spring to summer over the entire subtropical gyre. In the annual mean there is net EDW formation in the west to the south of the Gulf Stream, and net destruction over the eastern part of the gyre. Our results suggest that annual-mean formation rates of EDW associated with air-sea fluxes are in the range 3 to 5 Sv. Finally, error estimates are computed from sea-surface temperature and heat flux data using an ensemble perturbation method. It is found that transformation/formation patterns are robust and that errors mostly affect

integral quantities.

1. Introduction

The main purpose of the present study is to demonstrate how transformation and formation maps, inspired by Walin's (1982) integral water mass transformation framework, can be used to yield spatial and temporal information about water mass formation/destruction processes associated with air-sea fluxes. Conventional applications of Walin's approach yields *integral* statements about water mass transformation and formation rates based on air-sea fluxes integrated over outcrops. Here we demonstrate the utility of mapping out an appropriately defined "integrand" over the seasonal cycle to yield quantitative *regional and temporal* information about where and when water masses are formed. Brambilla et al. (2008) have recently used transformation maps to study North Atlantic Subpolar Mode Water. We use the same technique here but also investigate the utility of mapping formation as well as transformation rates.

To illustrate the method in an interesting and important context, we focus on the contribution of air-sea heat fluxes to the volume of water between 17°C and 19°C, which we call Eighteen Degree Water (EDW).[1] The thickness of the $18 \pm 1°$C layer is plotted from a new ocean atlas called OCCA (for OCean Comprehensive Atlas, as described in Section 3a, see also Forget 2008) in Fig.1-A. The layer is particularly thick south of the Gulf Stream: the annual mean depth of the 18°C surface is $\simeq$300m and its maximum thickness (centered around 35N/55W) varies from 450m in the late winter to 250m in the late summer. Argo profiles within the $10^o \times 5^o$ white box centered on 35N/55W marked in panel A, are plotted over three annual cycles in Fig.1-B. Data from the OCCA atlas, sampled to mimic the Argo

---

[1] Here we use the term "Eighteen Degree Water" in its literal sense and define it to be water with a temperature in the range $18 \pm 1°$C. It is not necessarily low potential vorticity water.

profiles, is shown in panel C. The Argo profiles and the OCCA atlas both clearly reveal the cycle of thickening and thinning of the EDW layer, which we now study using transformation and formation maps.

The paper is organized as follows: In Section 2 we describe how Walin's water mass framework can be used to create transformation and formation maps. In Section 3 we show how transformation and formation maps can be used to study Eighteen Degree Water (EDW). The datasets for which the maps are computed are described in Section 3a. In Section 3b the traditional Walin framework is used to describe water mass transformation and formation. Transformation and formation maps for EDW are analyzed in sections 3c and 3d. Section 4 provides an estimate of the errors in the maps. We conclude in section 5.

[Figure 1 about here.]

2. Formation and Transformation maps

Here we review how Walin's (1982) framework is used to quantify the rate at which water is transformed from one temperature class to another via air-sea heat fluxes (the transformation rate). The divergence of the transformation rate yields the rate at which a given temperature class is created or destroyed via air-sea heat fluxes (the formation rate). Because Walin's framework is an integral statement over temperature outcrops, it can describe the temporal evolution of transformation and formation rates, but at the expense of losing spatial information. In this section, we will discuss how we can create maps of transformation and formation rates, allowing us to retain crucial spatial information.

Consider the layer of water designated by Θ in a temperature range between: $\theta_1 < \theta < \theta_2$, which outcrops at the sea surface. The volume of the Θ layer is bounded by the isothermal surfaces θ_1 and θ_2 and above by the sea surface, see Fig.2. Following Walin (1982), the change in volume of the Θ layer is:

$$\frac{\partial V_\Theta}{\partial t} = A(\theta_2, t) - A(\theta_1, t) - M(\Theta, t) \tag{1}$$

where $A(\theta_i, t)$ is the diathermal volume flux across the isothermal surface $\theta_{i=1,2}$ and $M(\Theta, t)$ is the volume flux out of the control volume into the remainder of the ocean (see Fig.2). Positive (negative) values of A are toward cooler temperatures, directed mainly poleward (equatorward), and associated with cooling (warming).

Since advection can only deform a material surface in an incompressible, inviscid fluid, leaving the volume enclosed by it unchanged, A depends only on non-advective (interior diffusive and air-sea) fluxes. Separating the non-advective supply of heat to the volume into contributions associated with air-sea heat fluxes and interior diffusive processes, we write Walin's formula thus (following the notation introduced by Garrett et al. 1995; Marshall et al. 1999):

$$A(\theta, t) = F(\theta, t) - \frac{\partial D(\theta, t)}{\partial \theta} \tag{2}$$

where $D(\theta, t)$ is the diffusive flux of temperature across interior surfaces of the volume and

$$F(\theta, t) = \frac{\partial}{\partial \theta} \iint_{\theta_0}^{\theta} -\frac{Q_{net}}{\rho C_p} \, ds \tag{3}$$

is the contribution due to air-sea heat fluxes. Temperature θ_0 labels a reference surface (see

Fig.2), Q_{net} is the air-sea heat flux (positive upward) in Wm^{-2}, $\rho_o = 1035\,kg\,m^{-3}$ is the reference sea-surface density, $C_p = 4000\,J\,K^{-1}\,kg^{-1}$ is the specific heat capacity of water, ds is an area element at the sea surface. The term $F(\theta,t)$ is known as the *transformation rate* due to air-sea heat fluxes. It has units of m^3s^{-1} (and so can be expressed in Sverdrups where $1Sv = 10^6 m^3.s^{-1}$) and is a function of time and temperature θ. Like A, a positive transformation rate F indicates a transfer of water across θ from warm to cold temperatures and is thus associated with an increase of the volume between θ_0 and θ (see Fig.2-A).

A discretized expression for F is:

$$\begin{aligned} F(\theta,t) &= \frac{1}{\Delta\theta}\left(\iint_{\theta_0}^{\theta+\Delta\theta/2} -\frac{Q_{net}}{\rho C_p}\,ds - \iint_{\theta_0}^{\theta-\Delta\theta/2} -\frac{Q_{net}}{\rho C_p}\,ds\right) \\ &= \frac{1}{\Delta\theta}\iint_{\theta-\Delta\theta/2}^{\theta+\Delta\theta/2} -\frac{Q_{net}}{\rho C_p}\,ds \end{aligned} \tag{4}$$

and is an integral over a discrete isotherm outcrop, which is defined as the sea surface within the temperature class: $\theta \pm \frac{1}{2}\Delta\theta$.

We now re-write $F(\theta,t)$ as:

$$F(\theta,t) = \iint_{x,y} \mathcal{F}(t,x,y,\pi)\,ds \tag{5}$$

where

$$\mathcal{F}(t,x,y,\pi) = -\frac{Q_{net}(t,x,y)}{\rho C_p}\cdot\pi \tag{6}$$

is a two-dimensional map of the transformation rate F, in the sense that the surface integral of $\mathcal{F}$ will yield F.

The boxcar sampling function of temperature is defined as:

$$\pi(\theta_i, \Delta\theta) \quad = \quad \begin{cases} \frac{1}{\Delta\theta} & \text{if } \theta_i - \frac{\Delta\theta}{2} < \theta < \theta_i + \frac{\Delta\theta}{2} \\ 0 & \text{otherwise} \end{cases} . \tag{7}$$

The instantaneous 2D map of $\mathcal{F}$ is zero everywhere except over the outcrop window of the temperature class defined by $\pi_{\theta_i,\Delta\theta}$. However, when averaged in time (for example over a month or a year), the seasonal migration of the surface outcrops sweeps out a larger region, and patterns emerge in the map of $\overline{\mathcal{F}}$, as will be described in section 3c. Such an approach was recently proposed by Brambilla et al. (2008) and used in potential density coordinates to map transformation rates of North Atlantic Subpolar Mode Water.

The contribution of air-sea heat fluxes to the change in volume of water of the Θ layer is called the formation rate ΔF given by

$$\Delta F(\Theta, t) = F(\theta_2, t) - F(\theta_1, t) \tag{8}$$

and is obtained by taking the difference in the transformation rates across the bounding isothermal surfaces.

We can visualize spatially the contribution of air-sea heat fluxes by computing the difference between the transformation rate maps corresponding to the temperature classes $\pi_{\theta_2,\Delta\theta}$ and $\pi_{\theta_1,\Delta\theta}$ thus:

$$\Delta\mathcal{F} \quad = \quad \mathcal{F}(t, x, y, \pi_{\theta_2,\Delta\theta}) - \mathcal{F}(t, x, y, \pi_{\theta_1,\Delta\theta}). \tag{9}$$

$\Delta\mathcal{F}$ is called the formation rate map and has the property:

$$\Delta F \;=\; \iint_{x,y} \Delta\mathcal{F}\, ds. \tag{10}$$

Averaging $\Delta\mathcal{F}$ in time yields spatial maps which show where water of temperature range Θ is formed over a given period. Thus, the aforementioned mapping technique can be used in conjunction with Walin integral statements to reveal information about where and when a water mass is formed by air-sea interaction.

Note that Brambilla et al. (2008) questioned the feasibility of mapping formation rates as in Eq.(9). Here we hope to demonstrate the utility of formation maps by considering the volume of water within a finite temperature range: its volume is changed by the action of non-advective processes on the two isothermal surfaces that demarcate it.

To understand how the transformation and formation rate maps relate to Walin statements, let us consider the two isotherms θ_1 and θ_2, the northern and southern boundary of the layer Θ, shown schematically Fig.2-B in the horizontal and Fig.2-C in the vertical. We assume here that D and M are zero in Eqs.(1-2), so that there is a simple balance between the rate of volume change and formation/destruction by air-sea heat fluxes. Now suppose that there is more intense cooling occurring over the $\pi_{\theta_2,\Delta\theta}$ class than over $\pi_{\theta_1,\Delta\theta}$. Cooling induces the isotherms to migrate southward which corresponds to a positive (poleward) diathermal volume flux F. Since the diathermal volume flux across θ_2 is greater than across θ_1, the volume of the Θ layer increases (see black arrows in Figs. 2B and C). The two left panels shown in Fig.2-D represent the mapping of these transformation rates, according to Eq.(6). The formation rate map $\Delta\mathcal{F}$, sketched in Fig.2-D, shows the local rate of change in volume of the Θ layer.

[Figure 2 about here.]

3. Studying Eighteen Degree Water using Transformation and Formation maps

In this section we will use transformation and formation rate maps, in conjunction with the Walin formula, to study Eighteen Degree Water (EDW). We will define EDW to be the volume of fluid bounded by the isothermal surfaces $\theta_1 = 17^o C$ and $\theta_2 = 19^o C$. Thus, all water with temperature $\theta = 18 \pm 1^o C$ is included in our budget, not just weakly stratified waters. Two different datasets will be used, as described in the next section.

a. *Description of the datasets*

We choose here to work in temperature classes and so require estimates of sea surface temperatures (SST) and net air-sea heat fluxes (Q_{net}). There are many such data sets, whose relative merits and consistency are difficult to determine. Here we choose to focus on two SST and Q_{net} datasets, which have complementary qualities.

The first data set is OCCA, which was produced at MIT by the ECCO group and is available[2] for the data-rich Argo period 2004 to 2006. It is a global state estimate of the evolving state of the ocean on a $1^o \times 1^o$ horizontal grid with 50 vertical levels extending from the surface of the ocean to the bottom. It was produced using the MITgcm (Marshall et al.

---

[2] Online at: `http://www.ecco-group.org/`

1997a,b) data assimilation technology (ECCO) which fits the model trajectory as closely as is possible to all modern data sets, including Argo profiles, surface altimetry, and satellite SSTs. The fitting of the model to the data is done by sweeping backwards and forwards over 16 month periods using air-sea fluxes and winds as control variables. OCCA surface heat fluxes are computed via the Large and Pond (1981) bulk formulae using the model SST and NCEP-R1 analyzed fields of winds and atmospheric temperature and humidity, employing a surface boundary layer model. Three consecutive years are available, 'joined together' using linear interpolation over 4 months of overlap. This method has the notable advantage of confining spurious drifts of the model away from observations, yielding a state estimate that is very close to observations. A precise description of the resulting dataset can be found in Forget (2008).

Panels B and C in Figure 1 compare OCCA with raw Argo temperature profiles. Panel B is produced by plotting as a function of time every Argo temperature profile within a $10^o \times 5^o$ box centered on the EDW bowl at 35^oN/55^oW. Panel C shows the corresponding plot from OCCA, sampled accordingly. The EDW layer shows a seasonal cycle with a short period of wintertime ventilation when the 19°C isotherm reaches the surface and a longer period of re-stratification throughout the remainder of the year. Although the OCCA time series is smoother than that from Argo (largely due to the absence of eddies), the depth, thickness and temporal characteristics of the EDW layer are very similar in OCCA and Argo float data. Using OCCA , Forget et al. (2008a) have computed a volume budget of EDW using Eqs. (1-2). Here we use the OCCA air-sea heat flux and SST to illustrate our diagnostic technique.

The second dataset (hereafter MIXED) consists of SST maps and atmospheric state estimates produced by Remote Sensing System and the European Center for Medium-Range Weather Forecasts (ECMWF), respectively. SST maps are a blend of radiometer and microwave observations (TMI-AMSRE), with a native resolution of $1/4^o$ and one day (see `http://www.remss.com` for more details). Atmospheric state variables required to compute surface turbulent and radiative heat fluxes are taken from the ECMWF Operational system, which provides daily global gridded data from 1994 to the present. Atmospheric variables are linearly interpolated on to the satellite SST grid, and surface turbulent and radiative heat fluxes are then computed using the most recent Coupled Ocean-Atmosphere Response Experiment (COARE) bulk algorithm (version 3.0, Fairall et al. 2003), which has been shown to be "the least problematic" flux scheme relative to other algorithms (Brunke et al. 2003). The net surface heat flux is computed by summing turbulent and radiative fluxes from the COARE 3.0 algorithm. Such a method could lead to spurious local values, but a careful inspection of MIXED (see App.A) suggests that it yields reasonable estimates for the purpose of this study.

Daily data (2004 to 2006) from OCCA (1^o spatial resolution) and MIXED ($1/4^o$ spatial resolution) data are linearly interpolated onto a $1/8^o$ grid in order to avoid any bias in the temperature class sampling that would undermine comparison between them.

b. *Walin calculation*

Walin integral statements of the EDW water mass transformation rate and formation rate are computed using both the OCCA and MIXED datasets. Temperature classes are defined with a bin interval of $\Delta\theta = 1/2°\mathrm{C}$; for example, the 19°C temperature class consists of all points having a temperature θ such that $19 - 0.25 \leq \theta \leq 19 + 0.25$ (boxcar function $\pi_{19,1/2}$). Sensitivity of the results to this bin choice is discussed in App.B.

The 3-year time mean of $F(\theta)$ is shown in Fig.3-A for the temperature range $10^oC - 25^oC$. The gray shaded area emphasizes the EDW temperature range. Both datasets show a larger mean transformation rate at 19^oC than at 17^oC, implying production of EDW: $\overline{\Delta F}(18°\mathrm{C}) = \overline{F}(19°\mathrm{C}) - \overline{F}(17°\mathrm{C}) = 5.6Sv$ in OCCA and $3Sv$ in MIXED. These values are somewhat smaller than previous estimates based on Walin found in the literature, which range from about $10Sv$ to $20Sv$ (see Speer and Tziperman 1992; Speer et al. 1995; Nurser et al. 1999, for example). Computational details can account for a part of this wide range of values, but the main uncertainty is likely to be in the estimates of the net air-sea fluxes themselves. Resolution may also affect results, especially in calculations which were done at low spatial and temporal resolution (note that in our study, interpolation onto a $1/8^o$ grid reduced mean transformation rates by an amplitude of about $1Sv$).

Time series of $\Delta F(18°\mathrm{C})$ (net EDW formation rate) are shown in Fig.3-B. Formation rates calculated using both datasets exhibit a marked seasonal variability with daily formation rates reaching as high as $200Sv$ in winter (especially February) and $-50Sv$ (destruction) in summer. Both datasets produce a very similar seasonal cycle, but a larger wintertime formation rate is obtained using OCCA than using MIXED. The primary formation period is January to March and the primary destruction period is April to June. This is clearly seen in Fig.3-C, which shows the mean monthly formation rate over the three year period. The formation rate reaches a peak in February: $63Sv$ and $43Sv$ for the OCCA and MIXED datasets respectively. The formation rates calculated from the two datasets differ most during the formation period and are rather similar during the rest of the year. Fig.3-B also shows the interannual variability in $\Delta F(18°\mathrm{C})$ which is quantified in Fig.3-C as the standard deviation (STD) of monthly values over 3 years. The largest STD is found during the formation period, peaking at 19Sv for OCCA in February and 9Sv for MIXED in March.

The three year average formation rate due to air-sea heat fluxes is positive, indicating that more EDW is formed by air-sea heat fluxes than is destroyed. Forget et al. (2008a) found the volume of the EDW layer to be close to a steady state over the 2004-2006 period. This suggests that other processes (such as ocean mixing) act to destroy EDW. We will not consider these processes here, but the interested reader is referred to Forget et al. (2008a,b) for a discussion of the annual cycle of EDW volumes in OCCA and the contributing formation and dissipation processes.

[Figure 3 about here.]

c. *Mapping EDW Transformation rates*

Using Eq.(6) we mapped the mean transformation rate over the 3-year period for the temperature classes 19 ± 0.25^o and $17 \pm 0.25°\mathrm{C}$. The mean transformation rate maps are shown in Figure 4. By construction, the surface integral of the maps $\overline{\mathcal{F}}(19°\mathrm{C})$ and $\overline{\mathcal{F}}(17°\mathrm{C})$ yield the Walin transformation rates $\overline{F}(19°\mathrm{C})$ and $\overline{F}(17°\mathrm{C})$ shown in Fig.3-A.

[Figure 4 about here.]

Maps of transformation rates computed from both datasets and for each temperature class have the same general form: a meridional dipole with positive values in the south and negative values in the north of the domain swept out by the SST outcrops over the seasonal cycle. (Note that in Fig.4 the position of the outcrop in March and August is marked). Positive (negative) values imply a poleward (equatorward) transfer of water and are associated with cooling (warming).

The cause of the meridional dipole can be understood by calculating maps of seasonal average transformation rates. Figs. 5 show the average transformation map over wintertime (October to March with monthly outcrops marked) and summertime (April to September with monthly outcrops marked) for both datasets. Wintertime transformation maps are almost everywhere positive in OCCA (MIXED) yielding a wintertime transformation rate of $40\,Sv$ and $23\,Sv$ ($33\,Sv$ and $19\,Sv$) for 19 ± 0.25^oC and 17 ± 0.25°C. Summertime transformation maps are almost everywhere negative, and OCCA (MIXED) yield a summer transformation rate of $-22\,Sv$ and $-16\,Sv$ ($-22\,Sv$ and $-14\,Sv$) for 19 ± 0.25^o and 17 ± 0.25°C.

In areas where a temperature class outcrops in both the wintertime and the summertime, the wintertime cooling and summertime warming cancel out over the seasonal cycle, yielding near zero annual mean transformation rates for the temperature class. This cancellation explains the near zero transformation rates observed in the center of the region swept out by the outcrops over the seasonal cycle. However, in the southernmost and northernmost locations where a temperature class outcrops, no such cancellation occurs. Since an outcrop reaches its southernmost location during wintertime, the transformation rate in this region is dominated by wintertime cooling. Similarly, the transformation rate in the northernmost location of the outcrop is dominated by summertime warming. Thus, in maps of the annual mean transformation rate (Fig.4), a meridional dipole is observed. Note, however, the marked east-west asymmetry associated with both the fanning out of the outcrops on moving east across the basin, and the presence of intense air-sea fluxes in the region of the separated Gulf Stream.

[Figure 5 about here.]

Although the transformation rates for both the 19°C and 17°C temperature classes exhibit a meridional dipole, they also have important differences. $\overline{\mathcal{F}}(19°\text{C})$ exhibits a maximum over a wide area to the west of 45^oW between the Gulf Stream and 30^oN. In contrast $\overline{\mathcal{F}}(17^oC)$ exhibits a maximum which is confined to the Gulf Stream in the western part of the basin (see Fig.4). These differences are due to the different responses of the 19°C and 17°C isotherms to wintertime cooling. In response to wintertime cooling, the 19°C isotherm migrates southwestward (particularly in February and March), opening up a large area. Over most of this area, the 19°C isotherm does not outcrop during the summertime. Thus, the 19°C transformation rate over this entire region is dominated by wintertime cooling and is, therefore, large and positive. In contrast, in the western part of the basin the 17°C isotherm remains constrained to the Gulf Stream in wintertime, and the area of positive transformation rates is constrained to a small area along the southern flank of the Gulf Stream. The greater area of positive transformation rates for the 19°C temperature class compared to the 17°C temperature class is the reason for the large drop in the Walin transformation curves between 19°C and 17°C (see Fig. 3-A).

d. *EDW Formation rate maps*

A map of the net formation rate of EDW over the 3-year period, $\overline{\Delta\mathcal{F}}(18°\text{C})$, is obtained by subtracting the transformation rate maps for the 17°C temperature class from the transformation rate maps for the 19°C temperature class, as expressed in Eq.(9) and shown in Fig.6 for both datasets. By construction surface integrals of $\overline{\Delta\mathcal{F}}(18°\mathrm{C})$ yields the formation rate $\overline{\Delta F}(18°\mathrm{C}) = \overline{F}(19°\mathrm{C}) - \overline{F}(17°\mathrm{C})$ (see $F(\theta)$ in Fig.3-A). Positive (negative) areas correspond to net formation (destruction) of EDW. We see that EDW is formed over a wide region south of the Gulf Stream.

[Figure 6 about here.]

Insight into the formation rate maps can be obtained by looking again at the transformation rate maps for the 19°C and 17^oC temperature classes (see Fig. 4). We see that $\overline{\mathcal{F}}(19^oC)$ and $\overline{\mathcal{F}}(17^oC)$ are broadly similar, except to the south of the Gulf Stream in the western part of the basin where the 19^oC transformation map exhibits a large positive maximum. Thus, we see that EDW formation south of the Gulf Stream is primarily driven by positive transformation rates (cooling) across the warm flank (the 19^oC isotherm).

The EDW formation region is marked by the large dashed black box extending westward from 45^oW to 75^oW and northwards from 30^oN to the mean March position of the 17^oC isotherm. Inside this box, surface integrals of $\overline{\Delta\mathcal{F}}(18^oC)$ are $7.7\,Sv$ and $6.3\,Sv$ for the OCCA and MIXED datasets respectively. Integrating over the entire domain yield mean formation rates $\overline{\Delta F}(18^oC) = 5.6Sv$ and $\overline{\Delta F}(18^oC) = 3Sv$ for OCCA and MIXED respectively. Although differences in integrated values over the entire domain are larger than over the formation box, they may not be significant when note is taken of the (random) error bar of $\pm\,1Sv$ (see section 4).

EDW formation in the box has an interesting spatial structure. Figure 7 shows the annual mean $\overline{\Delta\mathcal{F}}(18^oC)$ zonally integrated over the formation box, plotted as a function of distance south of the northern boundary (defined as the March position of the 17^oC isotherm). The formation rate rapidly increases moving southward from the northern boundary, reaches a maximum at distances between 50km and 300km, and then slowly decreases to small values at distances greater than 600km. The bump at 100km found in the OCCA dataset but absent in MIXED, is due to high formation rates observed in the OCCA dataset in the western part of the formation box where the Gulf Stream separates from the coast. The Gulf Stream may be separating from the coast too abruptly in the OCCA dataset, which suggests that the bump may be spurious. Refined regional observations that the CLIMODE project aims to provide will aid resolving these questions.

[Figure 7 about here.]

The maps of the 3-year mean EDW formation rate show that EDW is formed by air-sea heat fluxes in a broad region south of the Gulf Stream in the western part of the basin, with maximum formation rates 50-300 km south of the position of the March 17^oC isotherm. The main formation region of EDW is mostly coincident with the thickest layer of EDW seen in Fig. 1-A. The formation region found in this study is broadly similar to the region with large subduction rates across the mixed layer base seen by Valdivieso Da Costa et al. (2005) in an eddy permitting numerical simulation (see their Fig.5-B). Peng et al. (2006) proposed another definition of the formation area of EDW as: "the region where the March mixed layer temperature ranges between 17^oC and 19^oC". This definition is less rigorous but also broadly matches the formation area seen in this study (see Fig.6).

Destruction of EDW by air-sea fluxes, on the other hand, occurs over a wide area in the eastern half of the basin. Comparing surface integral of $\overline{\Delta\mathcal{F}}(18^oC)$ over all regions where

$\overline{\Delta\mathcal{F}}$ is positive to surface integral of $\overline{\Delta\mathcal{F}}$ over all regions where $\overline{\Delta\mathcal{F}}$ is negative, we find the integral of the negative regions to be about $-2/3$ that of the positive regions. Therefore, in calculating $\overline{\Delta F}(18^oC)$ in the Walin integral framework, EDW destruction in the eastern part of the basin partially cancels EDW formation south of the Gulf Stream in the western part of the basin. Thus a basin integral Walin analysis does not convey underlying mechanisms because it blends together distant regions of formation and destruction rates. The mapping technique, instead, exposes this crucial spatial inheterogeneity.

Monthly mean formation rate maps were calculated in order to determine when EDW is formed and to help us understand how the yearly mean pattern is established. Figure 8 shows monthly mean maps of formation rates for January to April. In January, EDW formation is restricted to the Gulf Stream region since the EDW outcrop has not yet opened up to the south. In February the 19^oC isotherm sweeps southward toward the core of the subtropical gyre, inducing a large flux of water into the 17^oC-19^oC temperature range (positive transformation rate across the warmer flank). February is thus the period of maximum formation over the year (see Fig 3-C). The February surface integral over the entire domain of $\Delta F(18^oC)$ is $63Sv$ for the OCCA dataset and $43Sv$ for the MIXED dataset. Formation rates integrated only over the formation box are $75\,Sv$ for OCCA and $52\,Sv$ for MIXED. In March the 19^oC isotherm reaches westward to its greatest extent. Due to the different behavior of the 19^oC isotherm in the two datasets, there is a large discrepancy between formation rates calculated from the two datasets in March. In April air-sea heat fluxes change sign and EDW is eroded over the same region in which it was formed in February. EDW continues to be destroyed in May but largely in regions outside the formation box.

[Figure 8 about here.]

4. Sensitivity of transformation and formation to random errors in input fields

A notable result from the previous section is the good overall agreement between maps of transformation and formation rates obtained from our two datasets. There are detailed differences, however, which result in sizable differences in integrated values. There are many possible sources of error in such estimates. Here we focus on the contribution of random errors in SST and Q_{net}, assuming that errors in the input fields have zero time mean and prescribed covariances. We compute the probability distribution functions (PDF) that result from perturbing SST, Q_{net}, or both, in a large ensemble of N perturbations. Each perturbation is generated by applying a time/space diffusive filter to a random field with a normal distribution (Weaver and Courtier 2001) and scaled by a map of expected error standard deviation. This method allows one to generate evolving surface perturbations with chosen distributions of error variance and zonal, meridional and temporal decorrelation scales. We compute three ensembles of N = 500 perturbations in which only Q_{net} is perturbed, only SST is perturbed and both Q_{net} and SST are perturbed. We add the perturbations to OCCA fields and compute EDW transformation/formation rates, as described in section 2, on the 1×1 degree grid with $\Delta_\theta = 0.5^o C$. For each ensemble we then compute the PDF of integral and mapped transformation/formation rates.

For Q_{net} perturbations we choose decorrelation scales of 7 days/8^o/4^o in the temporal, zonal and meridional directions respectively; and 7 days/2^o/2^o for SST perturbations.

Anomaly patterns in Q_{net} are more coherent in the zonal than in the meridional direction (Romanou et al. 2006) while this is not the case for SST anomalies (Hosoda and Kawamura 2004; Dong et al. 2006). We scale Q_{net} perturbations by the RMS difference between NCEP-R1 and ECMWF Analysis heat fluxes. This map has an amplitude of 100-120$W.m^{-2}$ along the Gulf Stream core and 40-60$W.m^{-2}$ in the subtropical gyre, and has a very similar pattern to the RMS difference between MIXED and ECMWF heat fluxes shown in Fig.10-B. We scale SST perturbations by the RMS difference between the Reynolds OI-V2 (Reynolds and Smith 1994) and TMI-AMSRE SST products that is about 1^oC along the Gulf Stream (peaking locally at 2^oC), and 0.5^oC in the subtropical gyre. The spatial pattern is very similar to the RMS difference between the TMI-AMSRE and NCEP-RTG SSTs shown in Fig.10-A.

The PDFs of annual mean basin-integrated rates are shown for the first ensemble (only Q_{net} perturbed) in Fig.9. PDFs of F(17^oC) and F(19^oC) (panel A) have a standard deviation of 0.5Sv and 1Sv, respectively. We obtain 0.4Sv/0.9Sv in the second ensemble (only SST perturbed) and 0.6Sv/1.4Sv for the third (both Q_{net} and SST perturbed). These values differ from one another (since they are calculated by perturbing different quantities) but not to a great extent. Typical error estimates are 0.5Sv for F(17^oC) and 1Sv for F(19^oC). The variance of F(19^oC) is larger than that of F(17^oC) because the 19^oC isotherm sweeps out a larger area than does the 17^oC isotherm, and thus the volume flux across it is more sensitive to errors in Q_{net} and/or SST. Fig.9-B shows the PDFs of $\Delta F(18^oC)$ for the first ensemble. It has a standard deviation of 1Sv. The other two ensembles yield similar values.

Monthly values of ensemble mean and ensemble standard deviation are given for $\Delta F(18^oC)$ in table Fig.9-B for the first ensemble. Ensemble mean values are close to the ones shown in Fig.3-C despite differences in grid resolution. The standard deviation ranges from 7Sv in February, at the peak of formation, to 0.5Sv at the end of summer when the ensemble mean formation rate is zero. It is noteworthy that the ensemble mean formation rate only exceeds two standard deviations in Dec/Jan/Feb and Apr/May/Jun.

The spatial distribution in formation rate errors is shown in Fig.9-C for the first ensemble and Fig.9-D for the second (the third, not shown, has a pattern very similar to that of the second ensemble). Both ensembles show the error to be maximum along the Gulf Stream, albeit somewhat more homogeneously distributed in space in the first ensemble than the second. These maps are error estimates associated with formation rate maps given by Fig.6. We conclude that the patterns in Fig.6 are robust to random errors in Q_{net} and SST. This is especially clear for the box in the western basin showing large EDW formation south of the Gulf Stream, while the largest errors are confined to the path of the Gulf Stream.

Finally, it should be said that given the random errors estimated here are of order $1Sv$, the larger differences in formation and transformation rates obtained using MIXED as opposed to OCCA, must be due to systematic errors (such as bulk layer formulations) which are more difficult to quantify. An attempt is given in Forget et al. (2008a).

[Figure 9 about here.]

5. Conclusion

Maps of transformation and formation rates due to air-sea heat fluxes have been developed which complement, and can be used alongside, the integral statement of water mass transformation introduced by Walin (1982). Spatial maps of formation rate allow us to observe where and when water masses are formed or destroyed due to air-sea heat fluxes. The mapping approach has been applied to study the cycle of North Atlantic EDW formation and destruction using two different datasets, OCCA and MIXED, which yield broadly similar results.

Transformation rate maps show the spatial distribution of the rate at which water of one temperature class is transformed into another. For 19^oC and 17^oC temperature classes, transformation rate maps exhibit a meridional dipole with positive values to the south (associated with winter heat flux cooling), negative values to the north (summer warming), and thus near zero values to the center of the region swept out by SST outcrops over a seasonal cycle. Moreover, it is natural to view formation/destruction of EDW as the difference between diathermal volume fluxes in to and out of the layer. Thus formation rate maps were computed as differences between maps of transformation rates. They reveal that EDW forms primarily between the Gulf Stream and 30^oN, to the west of 45^oW. Finally, an ensemble perturbation method was used to determine the amplitude and distribution of random errors due to SST and Q_{net} uncertainties. The transformation/formation patterns revealed by the maps appear to be robust to random errors.

Although transformation rate maps of both temperature classes exhibit a meridional dipole, there is a key difference between them that intimately drives the EDW formation rate (both its pattern and integrated value). The transformation rate map across the 19^oC isotherm exhibits a maximum over a wide area between the Gulf Stream and 30^oN to the west of 45^oW. In contrast, the transformation rate map across 17^oC exhibits a maximum which is confined to a small area along the southern flank of the Gulf Stream. This difference implies a net positive volume flux of water into the EDW layer (a positive formation rate) which is not balanced by negative volume flux in other areas or seasons. Note that the formation of EDW occurs in February, when the 19^oC isotherm migrates southwestward, while the 17^oC remains confined to the Gulf Stream. This implies that the EDW formation is primarily driven by positive transformation rates across the warm flank of the EDW layer. A small fraction of the EDW that is formed in late winter is destroyed in April, as a result of negative transformation rates (warming) across the still-open 19^oC outcrop.

The largest destruction of EDW by air-sea fluxes occurs over an extensive region in the central-eastern part of the basin, driven by positive transformation rates across the 17^oC isotherm. Formation maps thus emphasize the limitation of the Walin framework if one is interested in the budget of weakly stratified EDW, i.e. the North Atlantic Subtropical Mode Water (NASTMW), typically defined as the least stratified fraction of the EDW layer. As NASTMW is located south of the Gulf Stream, in the core of the subtropical gyre, we surmise that the formation site of EDW is that of NASTMW. Destruction of EDW, however, is in the central-eastern basin where no sizable volume of NASTMW is found. Thus, formation maps suggest that a Walin analysis performed over the entire basin, as required by the theory, is perhaps a lower bound of the NASTMW formation rate induced by air-sea heat fluxes. A more accurate estimate of NASTMW formation rate may be the integral over the dashed black box in the western basin defined in Section 3d.

On very long timescales we expect EDW volume to be in steady state. Kwon and Riser (2004) found a clear balance between formation and destruction of NASTMW over 40 years of data (at a rate of $\pm 3.5 Sv$ with an error of $\pm 0.5 Sv$). However, they also observed large interannual variability (see also: Marsh et al. 2005; Old and Haines 2006) and so we might not expect to find the EDW layer in balance over the short period 2004-2006. Nevertheless, a volumetric census of the EDW layer in OCCA indicates that, perhaps surprisingly, it is almost in balance (about a 1Sv of volume storage over a seasonal cycle and on average for the 3 years, Forget et al. 2008a). Thus the $5.6Sv$ of EDW formed by air-sea fluxes (or $7.7Sv$ for the NASTMW box integral) must be balanced by other destructive processes. Since only non-advective processes can lead to water mass transformation, interior diffusive processes must be responsible for destruction of EDW. Vertical and horizontal mixing and/or horizontal diabatic eddy fluxes due to unresolved eddies (see Radko and Marshall 2004) may be important in destroying EDW. These processes will be discussed in forthcoming papers (Forget et al. 2008a,b) in which subsurface estimates from the OCCA atlas are used to calculate volumes and dissipation rates. There we extend the mapping technique to interior processes.

Finally, it is important to emphasize that we have focused here on the role of air-sea fluxes in changing the volume of water in the particular temperature range of EDW because of its association with subtropical mode water. In the study of subtropical mode water, however, one is perhaps further interested in the cycle of potential vorticity destruction and creation induced by air-sea fluxes. The focus of attention is then the flux of potential vorticity across the EDW isopycnal outcrop and its circulation within the gyre on the interior isopycnic surface. Mapping out the air-sea potential vorticity flux using techniques similar to that discussed here, will be the subject of a future study.

Acknowledgment Microwave OI SST data are produced by Remote Sensing Systems and sponsored by National Oceanographic Partnership Program (NOPP), the NASA Earth Science Physical Oceanography Program, and the NASA REASoN DISCOVER Project. Data are available at `www.remss.com`. This work was supported by NSF (CLIMODE) and NASA (ECCO2).

REFERENCES

Brambilla, E., L. D. Talley, and P. E. Robbins, 2008: Subpolar mode water in the North Eastern Atlantic. Part II: Origin and transformation. *J. Geophys. Res.*, **113**, doi:10.1029/2006JC004063.

Brunke, M. A., C. W. Fairall, X. Zeng, L. Eymard, and J. A. Curry, 2003: Which bulk aerodynamic algorithms are least problematic in computing ocean surface turbulent fluxes? *J. Climate*, **16**, 619–635.

Dong, S., J. Sprintall, and S. T. Gille, 2006: Location of the Antarctic polar front from AMSR-E satellite sea surface temperature measurements. *J. Phys. Oceanogr.*, **36**, 2075–2089, doi:10.1175/JPO2973.1.

Fairall, C., E. Bradley, J. Hare, A. Grachev, and J. Edson, 2003: Bulk parameterization of air–sea fluxes: Updates and verification for the COARE algorithm. *J. Climate*, **16**, 571–591.

Forget, G., 2008: Mapping ocean observations in a dynamical framework: a 2004-2006 ocean atlas. *J. Phys. Oceanogr.*, submitted.

Forget, G., G. Maze, M. Buckley, and J. Marshall, 2008: Observational estimates of the seasonal cycle of North Atlantic eighteen degree water volume . *J. Phys. Oceanogr.*, submitted.

Forget, G., G. Maze, and J. Marshall, 2008: Local conservation principle for global water mass analysis. *J. Phys. Oceanogr.*, submitted.

Garrett, C., K. G. Speer, and E. Tragou, 1995: The relationship between water mass formation and the surface buoyancy flux with application to Phillip's Read Sea model. *J. Phys. Oceanogr.*, **25**, 1696–1705.

Hosoda, K. and H. Kawamura, 2004: Global space-time statistics of sea surface temperature estimated from AMSR-E data. *Geophys. Res. Lett.*, **31**, doi:10.1029/2004GL020317.

Kwon, Y. and S. Riser, 2004: North Atlantic subtropical mode water: A history of ocean-atmosphere interaction 1961–2000. *Geophys. Res. Lett.*, **31**, doi:10.1029/2004GL021116.

Large, W. G. and S. Pond, 1981: Open ocean momentum flux measurements in moderate to strong winds. *J. Phys. Oceanogr.*, **11**, 324–336.

Marsh, R., S. Josey, A. Nurser, B. de Cuevas, and A. Coward, 2005: Water mass transformation in the North Atlantic over 1985-2002 simulated in an eddy-permitting model. *Ocean Science*, **1**, 127–144.

Marshall, J., A. Adcroft, C. Hill, L. Perelman, and C. Heisey, 1997a: A finite-volume, incompressible Navier Stokes model for studies of the ocean on parallel computers. *J. Geophys. Res.*, **102**, 5753–5766.

Marshall, J., C. Hill, L. Perelman, and A. Adcroft, 1997b: Hydrostatic, quasi-hydrostatic, and nonhydrostatic ocean modeling. *J. Geophys. Res.*, **102**, 5733–5752.

Marshall, J., D. Jamous, and J. Nilsson, 1999: Reconciling thermodynamic and dynamic methods of computation of water-mass transformation rates. *Deep-Sea Res.*, **46**, 545–572.

Nurser, A. J. G., R. Marsh, and R. G. Williams, 1999: Diagnosing water mass formation from air-sea fluxes and surface mixing. *J. Phys. Oceanogr.*, **29**, 1468–1487.

Old, C. and K. Haines, 2006: North Atlantic subtropical mode waters and ocean memory in HADCM3. *J. Climate*, **19**, 1126–1148.

Peng, G., E. Chassignet, Y. Kwon, and S. Riser, 2006: Investigation of variability of the North Atlantic Subtropical Mode Water using profiling float data and numerical model output. *Ocean Modelling*, **13**, 65–85.

Radko, T. and J. Marshall, 2004: Eddy-induced diapycnal fluxes and their role in the maintenance of the thermocline. *J. Phys. Oceanogr.*, **34**, 372–383.

Reynolds, R. and T. Smith, 1994: Improved global sea surface temperature analyses using optimum interpolation. *J. Climate*, **7**, 929–948.

Romanou, A., W. B. Rossow, and S.-H. Chou, 2006: Decorrelation scales of high-resolution turbulent fluxes at the ocean surface and a method to fill in gaps in satellite data products. *J. Climate*, **19**, 3378–3393.

Speer, K., H. Isemer, and A. Biastoch, 1995: Water mass formation from revised COADS data. *J. Phys. Oceanogr.*, **25**, 2444–2457.

Speer, K. G. and E. Tziperman, 1992: Rates of water mass formation in the North Atlantic ocean. *J. Phys. Oceanogr.*, **22**, 93–104.

Taylor, K., 2001: Summarizing multiple aspects of model performance in a single diagram. *J. Geophys. Res.-Atmospheres*, **106**.

Valdivieso Da Costa, M., H. Mercier, and A. M. Treguier, 2005: Effects of the mixed layer time variability on kinematic subduction rate diagnostics. *J. Phys. Oceanogr.*, **35**, 427–443.

Walin, G., 1982: On the relation between sea-surface heat flow and thermal circulation in the ocean. *Tellus*, **34**, 187–195.

Weaver, A. and P. Courtier, 2001: Correlation modelling on the sphere using a generalized diffusion equation. *Quart. J. Roy. Meteor. Soc.*, **127**, 1815–1846.

A. The MIXED heat flux

The MIXED heat flux dataset was computed using TMI-AMSRE SST and ECMWF Analysis atmospheric state estimates. Atmospheric variables were linearly interpolated on to the satellite SST grid, and surface turbulent and radiative fluxes were then computed. Possibly incompatible SST and atmospheric states can lead to unrealistic results. The SST used in the ECMWF Analysis system is the NCEP Real-Time Global (RTG) produced with a two-dimensional variational interpolation analysis of the most recent 24-hour buoy and ship data, satellite-retrieved NOAA-17 AVHRR SST data, and SST's derived from satellite-observed sea-ice coverage. Fig.10-A shows the daily centered root-mean squared difference (RMSD) between the RTG-SST used by ECMWF and the TMI-AMSRE SST used here to produce MIXED. The two products differ most along the Gulf Stream with RMSD values of 1^oC, peaking locally at 2^oC. The RMSD between Q_{net} obtained from ECMWF and MIXED is shown in Fig.10-B. Differences are again largest along the Gulf Stream with values reaching $125W.m^{-2}$. Reassuringly this is of the same order of magnitude and spatial scale as the RMSD between ECMWF and NCEP-R1 original heat fluxes[3] (not shown). This suggests that the MIXED heat flux does not contain spurious values and is as *different* from ECMWF as is NCEP.

We also compared time mean values of Q_{net} from MIXED with other datasets. Results are summarized in Fig.10-C which plots the zonal mean and time mean of the monthly time series of Q_{net} from National Oceanographic Center version 1.1 (NOC1.1) and the 2004-2006 daily time series from ECMWF, MIXED, OCCA and NCEP-R1. Relative to NOC1.1,

---

[3] Note that the RMSD between OCCA and NCEP-R1 heat fluxes is also very similar to the patterns shown here.

ECMWF and NCEP heat fluxes overestimate the oceanic heat loss in the latitude band of interest in mode water formation (30N to 45N). MIXED is closer to NOC 1.1 than, for example, ECMWF and so can be considered acceptable.

Last, we estimated the performance of the MIXED heat flux locally. The CLIMODE project deployed a meteorological buoy in the core of the Gulf Stream path at 38.5N/65W (denoted by a black cross on Fig.10-A and B) from which we compared daily sea surface heat fluxes with estimates from MIXED, OCCA, ECMWF and NCEP for the overlapping period of November 2005 to November 2006. The results are shown in a Taylor diagram in Fig.10-D (Taylor 2001). Each point represents a local time series (labeled A, B, C and D for the 4 global heat flux products, see legend in Fig.10-C). The distance from the center of the disk is the standard deviation (STD) and the angle from the x-axis is the correlation with the time series at the buoy. Thus the distance between the buoy point on the x-axis and other estimates is the RMSD between the time series. We see that ECMWF and MIXED have a similar STD to the buoy time series while OCCA underestimates it and NCEP overestimates it.

Global and local variabilities also with time mean of the MIXED heat flux was shown to be realistic, compared to several state of the art heat flux products. The point of this study is not to provide and present yet another heat flux product (MIXED is not aimed to be distributed), it is to compare formation maps from the OCCA dataset to maps obtained from another combination of SST and Q_{net} with a smaller spatial resolution. One important results of this study is the remarkable consistency of the patterns in formation maps despite the differences in basin integrated values.

[Figure 10 about here.]

B. Sensitivity to bin size and resolution

The numerical discretization of the transformation rate expression Eq. (4), make use of a temperature bin $\Delta\theta$ to define temperature classes. If the bin is too small there will be insufficient outcropping regions to resolve, leading to considerable noise in both maps and integral values. On the other hand, if the bin is too large we will lose ability to resolve temperature classes of interest. We found $\Delta\theta = 0.5^oC$ and a resolution of $1/8^o$ to be a good compromise leading to smooth maps which can resolve details.

To test the sensitivity of the formation rate value to the bin and resolution, we used various bins in the range 1^oC to $1/8^oC$ with several spatial resolutions in OCCA for 2005 only (for numerical efficiency reasons) to compute the EDW formation rate. Results are summarized in table 1. Whatever the spatial resolution, as the bin decreases, positive and negative area integrals tend to increase in amplitude. This reduces the error in resolving the temperature class (see Eq.B1) but also leads to average very large positive and negative values, increasing uncertainties. However, when a linear spatial interpolation is used to increase the horizontal resolution we see that the variability of the formation rate as a function of the bin decreases, and that for a given bin, the formation rate converges as the resolution increases. From table 1, the 2005 mean formation rate of EDW ranges from $5.1Sv$ to $7.48Sv$. For the range of bin and resolution used here, the mean value is $5.8Sv$ and the standard deviation among them is $0.5Sv$, which gives an estimate of the sensitivity of the results to the bin and resolutions of surface fields.

Finally we address the question of the discretization error of isotherms, ie the error in approximating an isotherm by a temperature class. This error is given by the difference between grid cell temperatures and the actual isotherm to be determine:

$$\mathcal{F}_e = -\frac{Q_{net}}{\rho C_p}\pi_{\Delta\theta,\theta_i} \cdot |\theta - \theta_i| \tag{B1}$$

Note that compared to Marshall et al. (1999) we chose to apply an absolute value to the difference $\theta - \theta_i$ in order to avoid spurious cancellation of errors. This gives an upper band on the error estimates. Maps and integral values of transformation and formation rates have been computed for $\mathcal{F}_e$ and $\Delta\mathcal{F}_e$ (not shown). We found this source of error to be: $0.4Sv$, $1.1Sv$ and $0.8Sv$ for $F(17^oC)$, $F(19^oC)$ and $\Delta F(18^oC)$ respectively. The mapping showed that this error has a similar distribution to the mean field and therefore acts to reinforce or weaken the pattern.

[Table 1 about here.]

List of Figures

2 Panel A: Schematic of the control volume bounded by isotherms θ_1 and θ_2, which is the subject of Walin's (1982) theoretical framework. V_Θ is the volume of the layer Θ, F and $\partial_\theta D$ are the surface and internal diathermal volume flux components, $M(\Theta)$ is the flow out of the control volume and vertical gray arrows represent air-sea fluxes. Temperature θ_0 labels a reference surface. Panel B-C: horizontal and vertical views of the two isotherms bounding the Θ layer with a non uniform meridional profile of heat flux cooling (letter c). Black arrows represent the diathermal volume flux across isotherms. Panel D: from the left to the right: maps of transformation rates across θ_1, θ_2 and formation rate of the Θ layer, time integrated between t and $t + dt$. Thick contours correspond to consecutive isotherm positions (thin contours demarcate associated temperature classes) and positive/negative signs denote areas of positive/negative rates. 41

7 Zonal integration of the mean formation map over the black dashed formation box in Fig 6, plotted as a function of the distance from its northern boundary (March monthly mean 17^oC isotherm). Plain: OCCA dataset, dashed: MIXED dataset. 46

8 January to April monthly mean formation maps $\overline{\Delta\mathcal{F}}(18^oC) = \overline{\mathcal{F}}(19^oC) - \overline{\mathcal{F}}(17^oC)$ for the three year period 2004-2006, in $Sv.m^{-2}$. Left: OCCA, right: MIXED. Blue contours are the 19^oC and 17^oC outcrops for each month. Green contours are the mean $-0.2m$ and $-0.6m$ SSH from OCCA. The box marked by the black dashed line encloses the main formation area of EDW. Integral quantities of the fields are shown in the upper left corner of each map in Sv: over the total domain (T), positive areas only (P), negative areas only (N) and over the dashed black box (B). A non-linear color scale has been used to reveal patterns. 47

9 From the OCCA dataset: PDFs of transformation $F(17^oC)$, $F(19^oC)$ (panel A) and formation $\Delta F(18^oC)$ (panel B) rates for the first ensemble experiment where only the air-sea heat flux is perturbed (see text). In Panel B, monthly mean and standard deviation of $\Delta F(18^oC)$ are tabulated. Lower panels: maps of local standard deviation of $\Delta F(18^oC)$ for the first (panel C) and second (panel D) ensemble with perturbations on Q_{net} and SST only respectively. Dashed black line is the formation box area and two thick black contours are mean $-0.2m$ and $-0.6m$ SSH from OCCA. 48

10 Panel A: RMS difference between daily TMI-AMSRE and RTG SSTs from 2004 to 2006. Panel B: RMS difference between daily MIXED and ECMWF Analysis sea-surface heat fluxes from 2004 to 2006. Panel C: Zonal mean of sea-surface net heat fluxes time mean from the National Oceanographic Center Version 1.1 (from 1991 to 2005, monthly fields), ECMWF Analysis (2004-2006, daily fields), MIXED (2004-2006, daily fields), OCCA (2004-2006, daily fields) and NCEP-R1 (2004-2006, daily fields). Panel D: Taylor diagram from local daily sea-surface net heat fluxes at the CLIMODE mooring localized at 38.5N/65W and denoted as the white cross in panels A and B. Individual points A, B, C and D stand for ECMWF, MIXED, OCCA and NCEP datasets respectively.

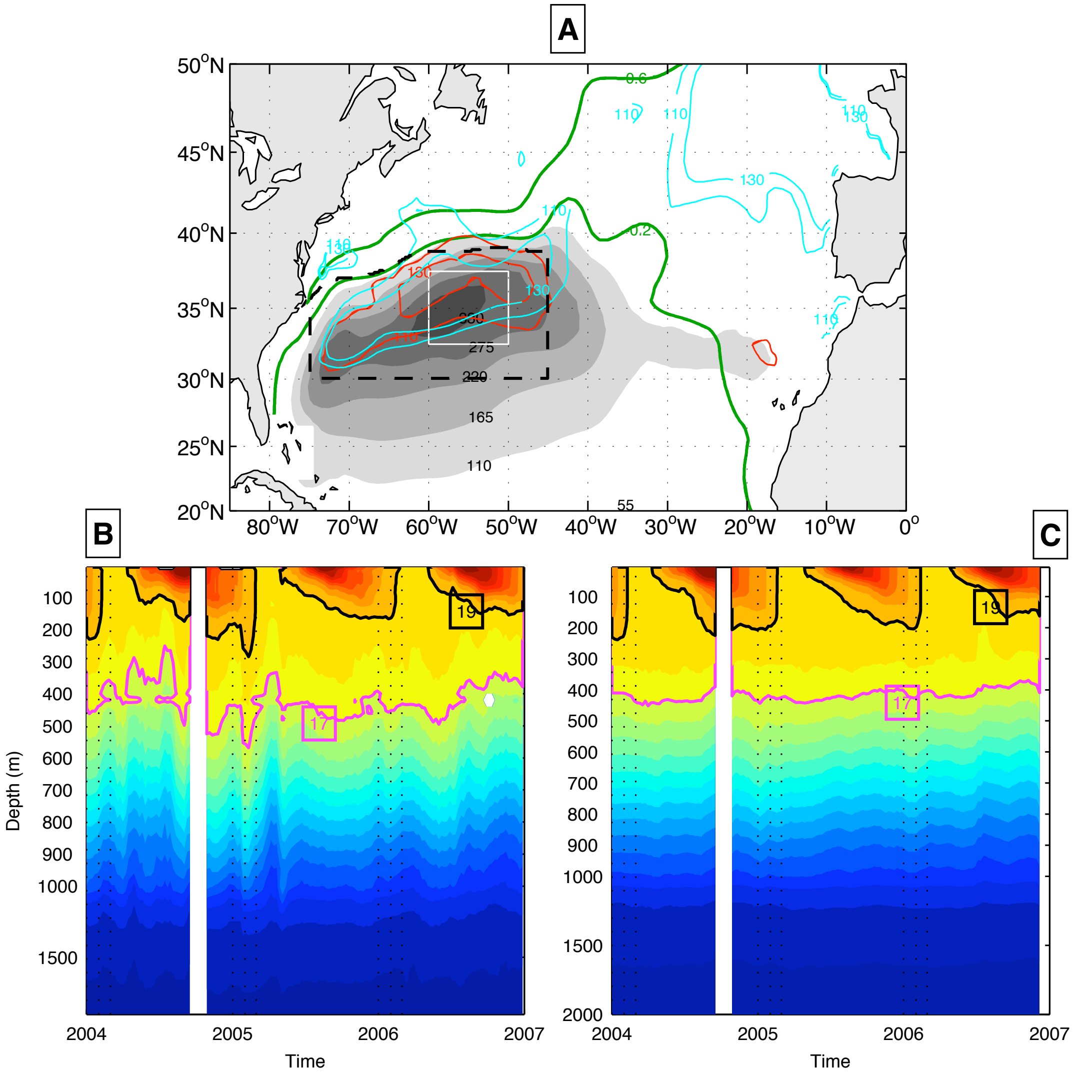

Figure 1: Panel A: Observed three-year (2004-2006) mean characteristics of the 18 ± 1^oC layer in the OCCA dataset. Mean thickness (shaded gray), monthly thickness standard deviation (red contours) and mixed layer depth standard deviation (blue contours). The two thick green contours are mean SSH (-0.2m;-0.6m), chosen to mark the arc of the subtropical and subpolar gyre. The box marked by the black dashed line encloses the main formation area of EDW (see section 3d). In Panel B: Every Argo profile within the $10^o \times 5^o$ white box centered on 35N/55W shown in panel A, is plotted as a function of time, beginning in January 2004 and ending in December 2006. The white bar indicates a period of time when there were no profiles. The 19^oC and 17^oC isotherms, enhanced in black and magenta, are plotted. The first day of January, February and March in each of the years is indicated by the vertical dotted lines. Panel C: As in Panel B but sampling the OCCA data set to mimic Argo profiles.

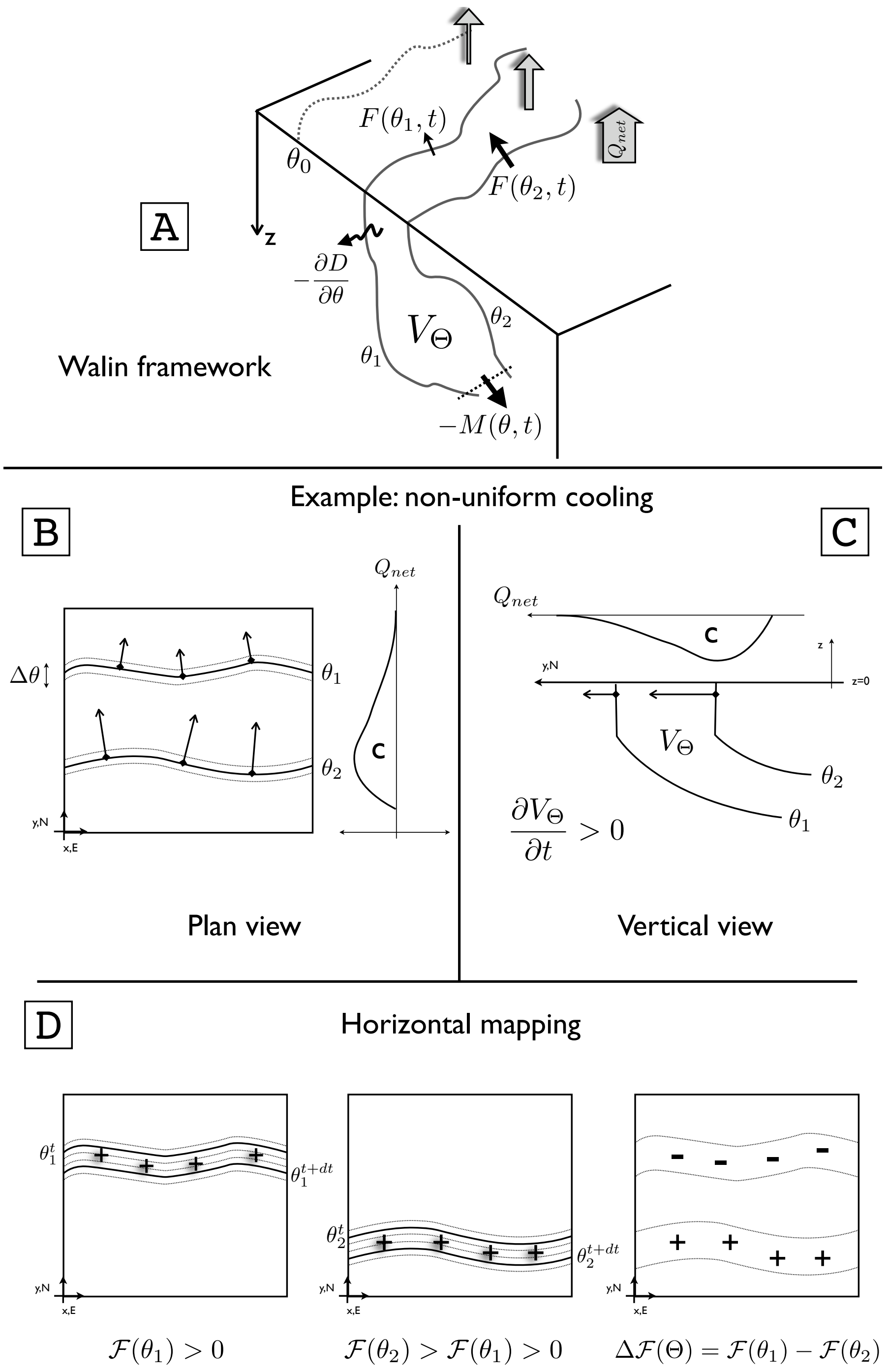

Figure 2: Panel A: Schematic of the control volume bounded by isotherms θ_1 and θ_2, which is the subject of Walin's (1982) theoretical framework. V_Θ is the volume of the layer Θ, F and $\partial_\theta D$ are the surface and internal diathermal volume flux components, $M(\Theta)$ is the flow out of the control volume and vertical gray arrows represent air-sea fluxes. Temperature θ_0 labels a reference surface. Panel B-C: horizontal and vertical views of the two isotherms bounding the Θ layer with a non uniform meridional profile of heat flux cooling (letter c). Black arrows represent the diathermal volume flux across isotherms. Panel D: from the left to the right: maps of transformation rates across θ_1, θ_2 and formation rate of the Θ layer, time integrated between t and $t + dt$. Thick contours correspond to consecutive isotherm positions (thin contours demarcate associated temperature classes) and positive/negative signs denote areas of positive/negative rates.

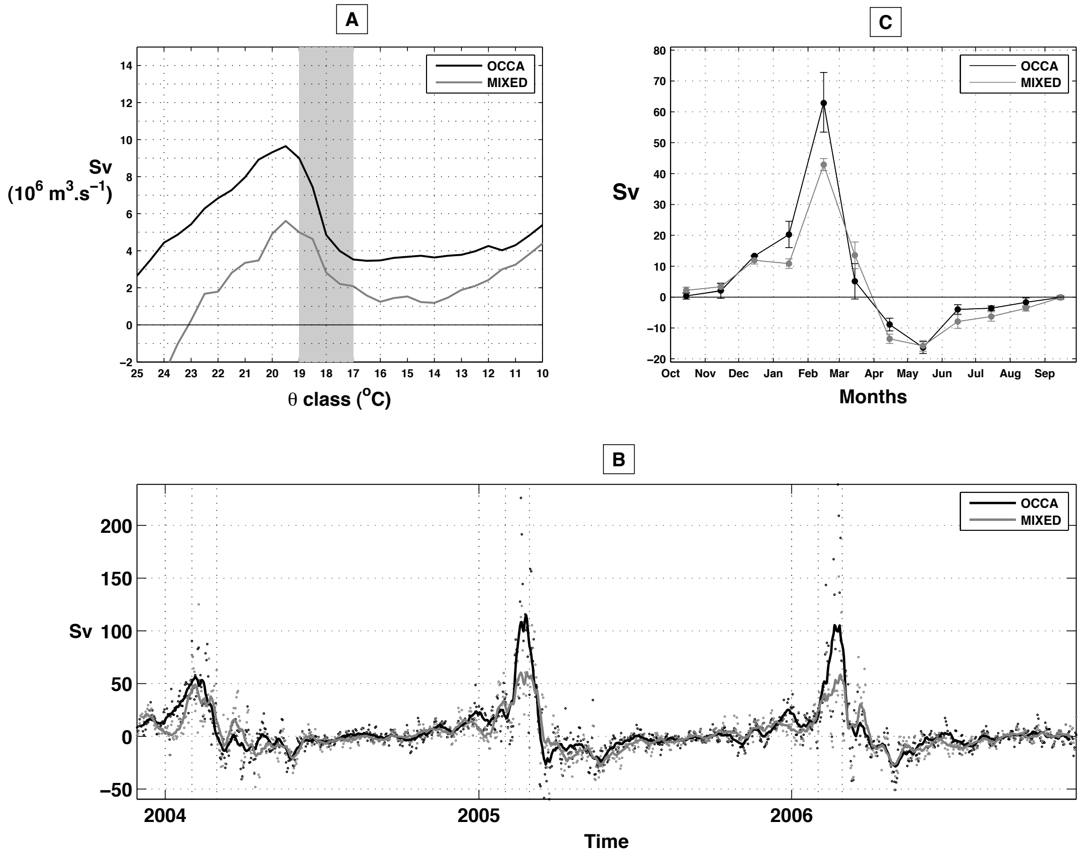

Figure 3: Panel A: Three years (2004-2006) mean transformation rates $\overline{F(\theta)}$ in OCCA (black) and MIXED (gray) datasets. The shaded area indicates the EDW range between 19^oC and 17^oC. Panel B: 2004-2006 time series of EDW formation rate $\Delta F = F(19) - F(17)$. Plain lines are daily time series which have been low-pass filtered with a 7 day cut-off frequency. Light black and gray dots are daily values for OCCA and MIXED datasets. First day of January, February and March are denoted by the vertical dashed lines at the beginning of each year. Panel C: Composite net formation rate $\Delta F(18^oC)$ obtained by averaging monthly mean fields over the three year timeseries shown in Panel B. Vertical bars mark the three year standard deviation amplitude. Circles are the values obtained by integrating in space monthly mean formation maps, such as those shown in Figure 8.

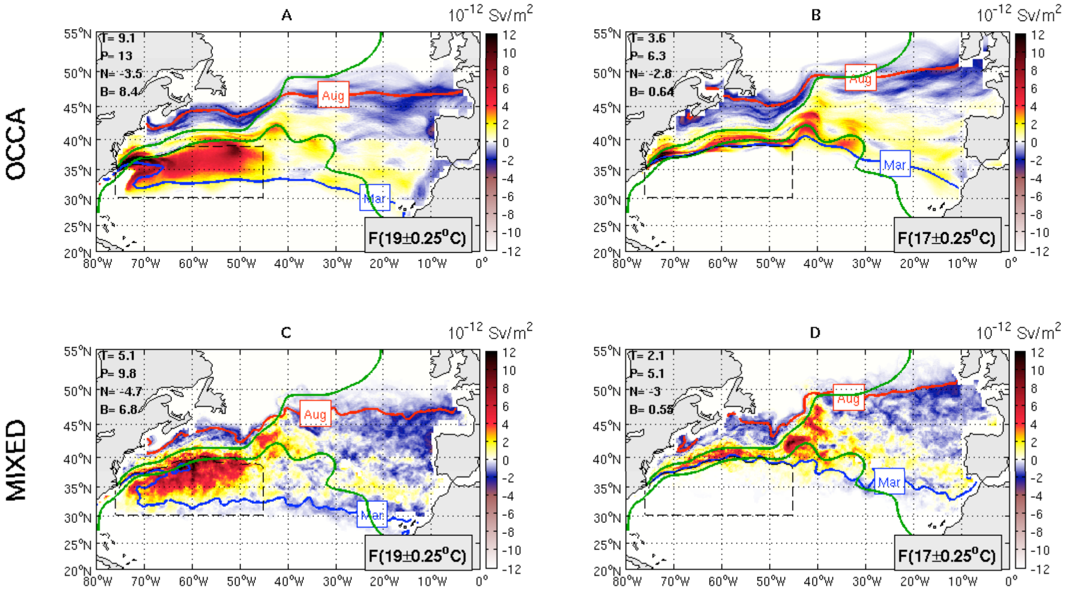

Figure 4: The mean transformation maps for the three year period 2004-2006, in $Sv.m^{-2}$. Left: $\overline{\mathcal{F}}(19^oC)$, Right: $\overline{\mathcal{F}}(17^oC)$. Top: OCCA dataset, bottom: MIXED dataset. Red and blue contours are the August and March mean position of the 19^oC (left) and 17^oC (right) isotherms. Green contours are the mean $-0.2m$ and $-0.6m$ SSH from OCCA. Integral quantities of the fields are shown in the upper left corner of each map in Sv: over the total domain (T), positive areas only (P), negative areas only (N) and over the dashed black box (B). A non-linear color scale has been used to reveal patterns.

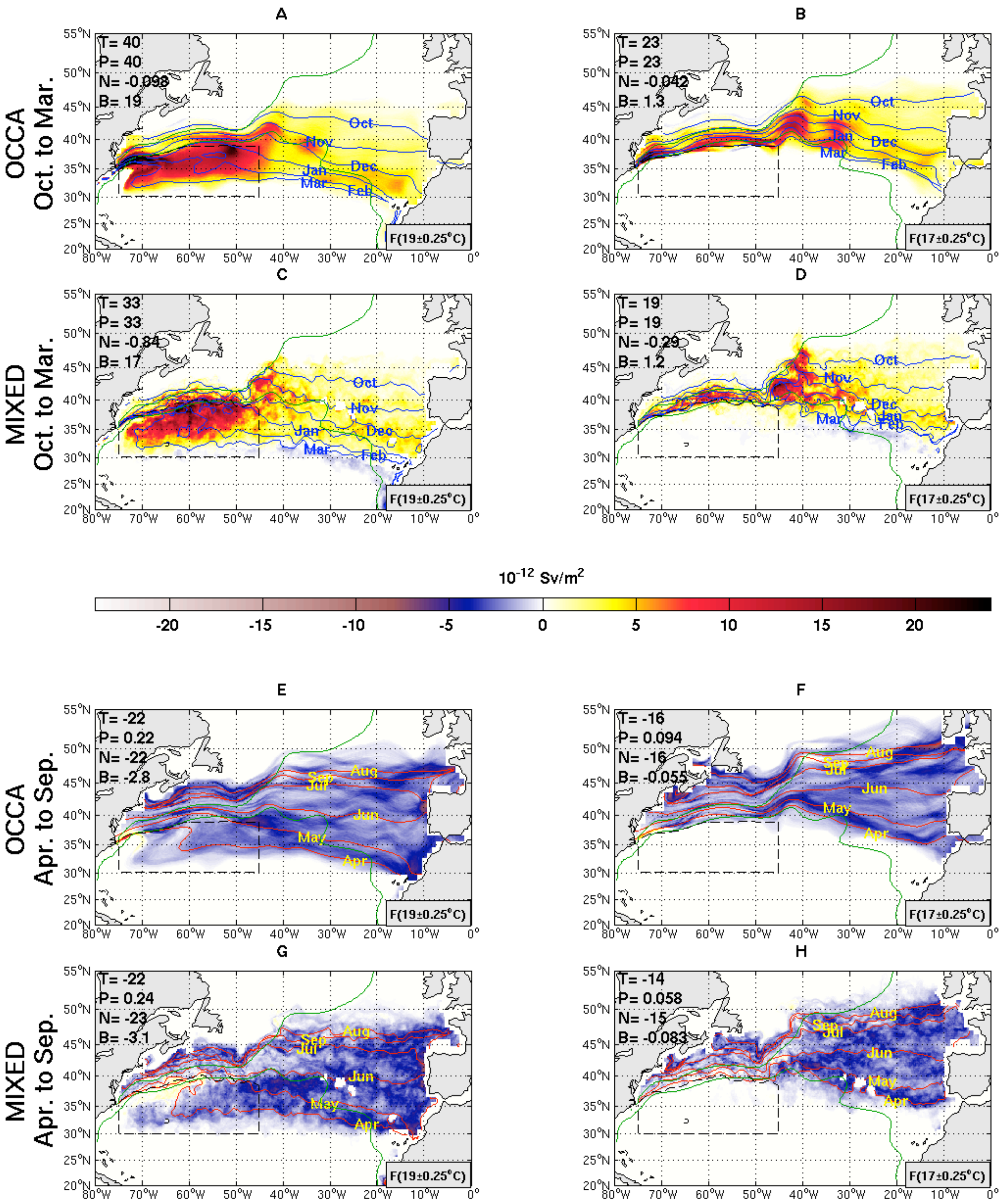

Figure 5: Maps A to D: Mean October-March (fall-winter) transformation maps for the three year period 2004-2006, in $Sv.m^{-2}$. Maps E to H: Mean April-September (summer-spring) transformation maps for the three year period 2004-2006, in $Sv.m^{-2}$. Left (A,C,E,G): $\overline{\mathcal{F}}(19^oC)$, Right (B,D,F,H): $\overline{\mathcal{F}}(17^oC)$. Top (A,B,E,F): OCCA dataset, bottom (C,D,G,H): MIXED dataset. Blue (resp, red) contours in maps A to D (resp, E to H) are the monthly mean positions for October to March (resp, April to September) of the 19^oC (left maps) and 17^oC (right maps) isotherms. Green contours are the mean $-0.2m$ and $-0.6m$ SSH from OCCA. Integral quantities of the fields are shown in the upper left corner of each map in Sv: over the total domain (T), positive areas only (P), negative areas only (N) and over the dashed black box (B). A non-linear color scale has been used to reveal patterns.

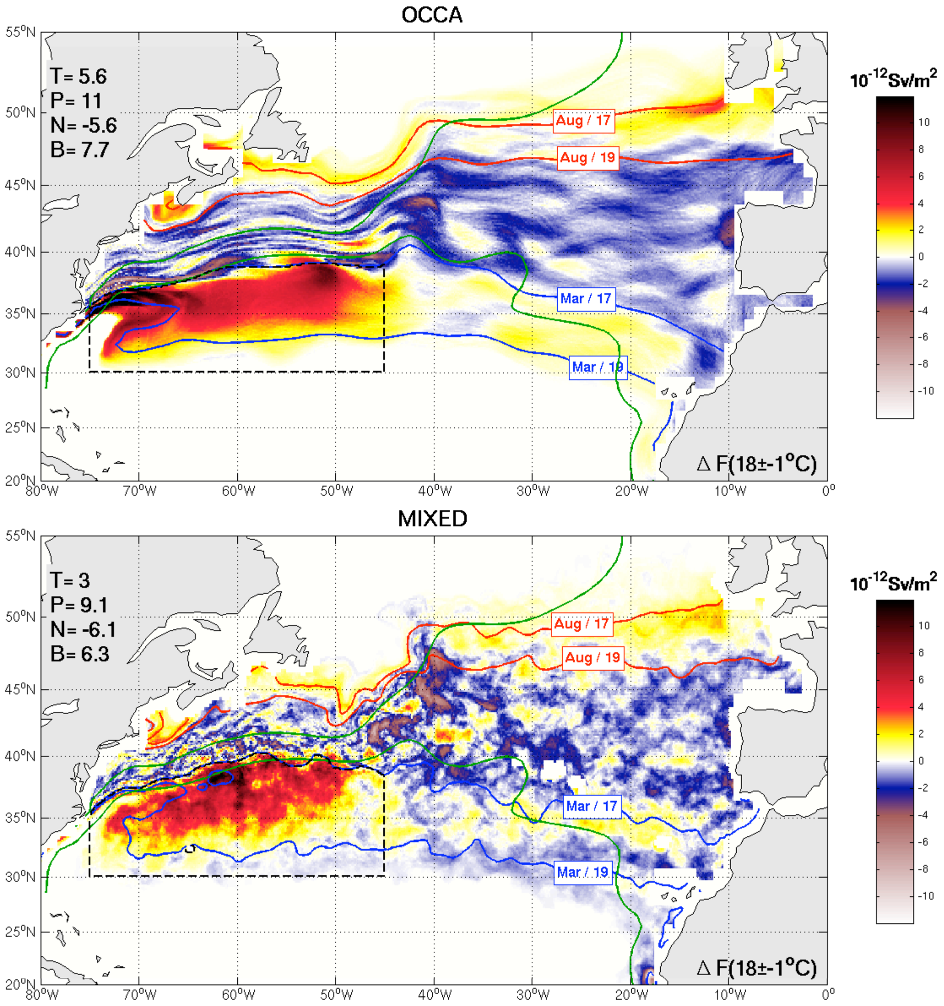

Figure 6: The mean formation maps $\overline{\Delta\mathcal{F}}(18^oC) = \overline{\mathcal{F}}(19^oC) - \overline{\mathcal{F}}(17^oC)$ for the three-year period 2004-2006, in $Sv.m^{-2}$. Top: OCCA dataset, bottom: MIXED dataset. Red and blue contours are the August and March mean position of the 19^oC and 17^oC isotherms. Green contours are the mean $-0.2m$ and $-0.6m$ SSH from OCCA. The box marked by the black dashed line encloses the main formation area of EDW. Integral quantities of the fields are shown in the upper left corner of each map in Sv: over the total domain (T), positive areas only (P), negative areas only (N) and over the dashed black box (B). A non-linear color scale has been used to reveal patterns.

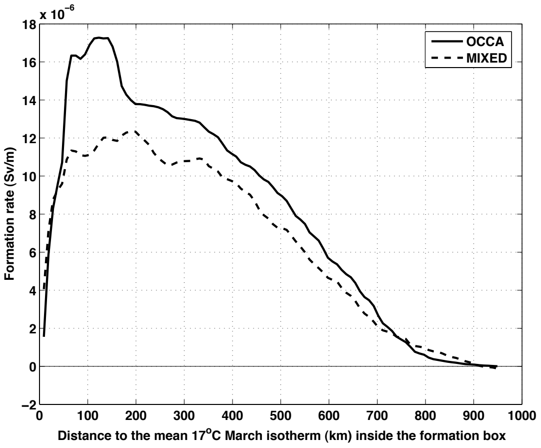

Figure 7: Zonal integration of the mean formation map over the black dashed formation box in Fig 6, plotted as a function of the distance from its northern boundary (March monthly mean 17^oC isotherm). Plain: OCCA dataset, dashed: MIXED dataset.

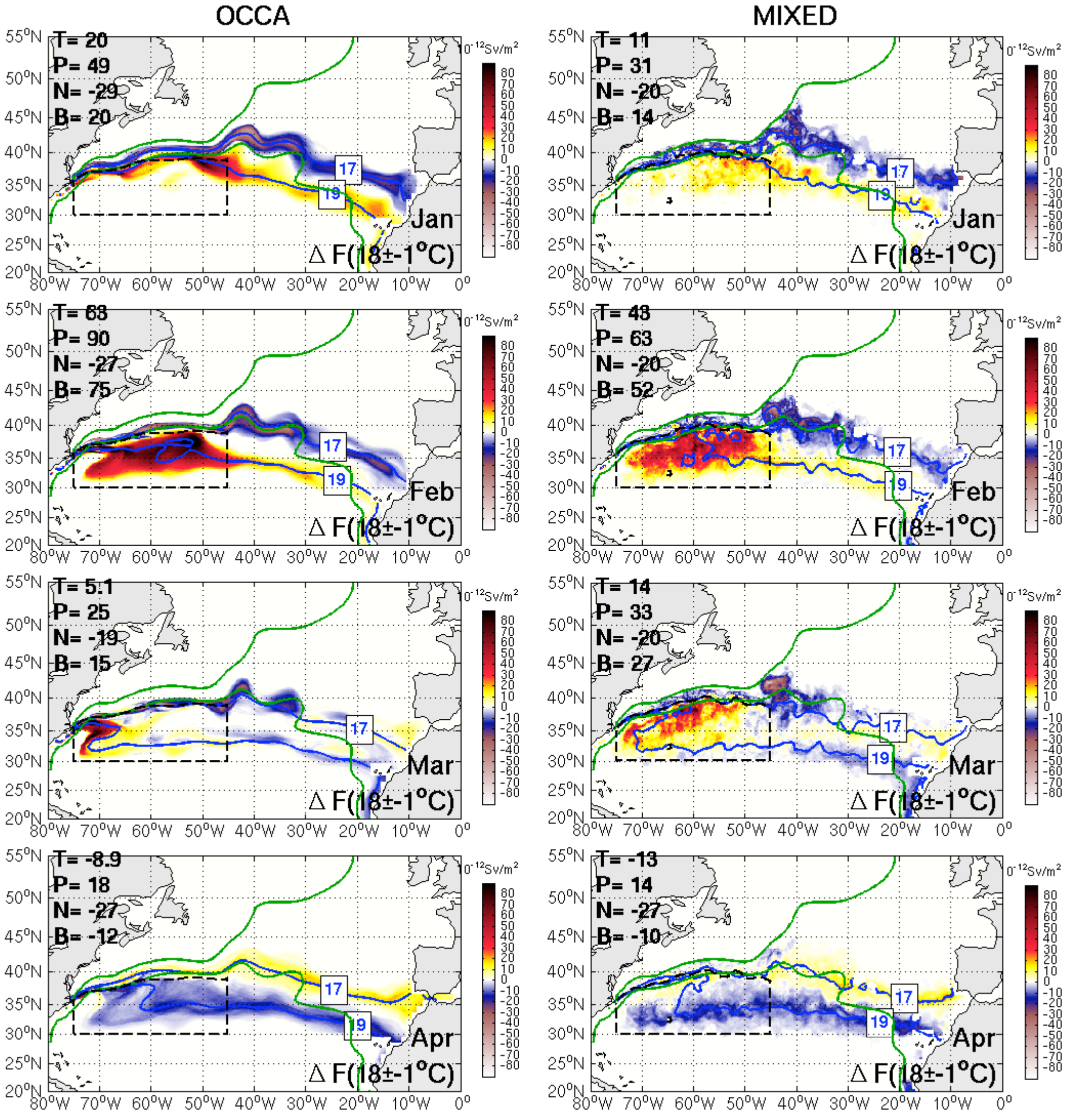

Figure 8: January to April monthly mean formation maps $\overline{\Delta\mathcal{F}}(18^oC) = \overline{\mathcal{F}}(19^oC) - \overline{\mathcal{F}}(17^oC)$ for the three year period 2004-2006, in $Sv.m^{-2}$. Left: OCCA, right: MIXED. Blue contours are the 19^oC and 17^oC outcrops for each month. Green contours are the mean $-0.2m$ and $-0.6m$ SSH from OCCA. The box marked by the black dashed line encloses the main formation area of EDW. Integral quantities of the fields are shown in the upper left corner of each map in Sv: over the total domain (T), positive areas only (P), negative areas only (N) and over the dashed black box (B). A non-linear color scale has been used to reveal patterns.

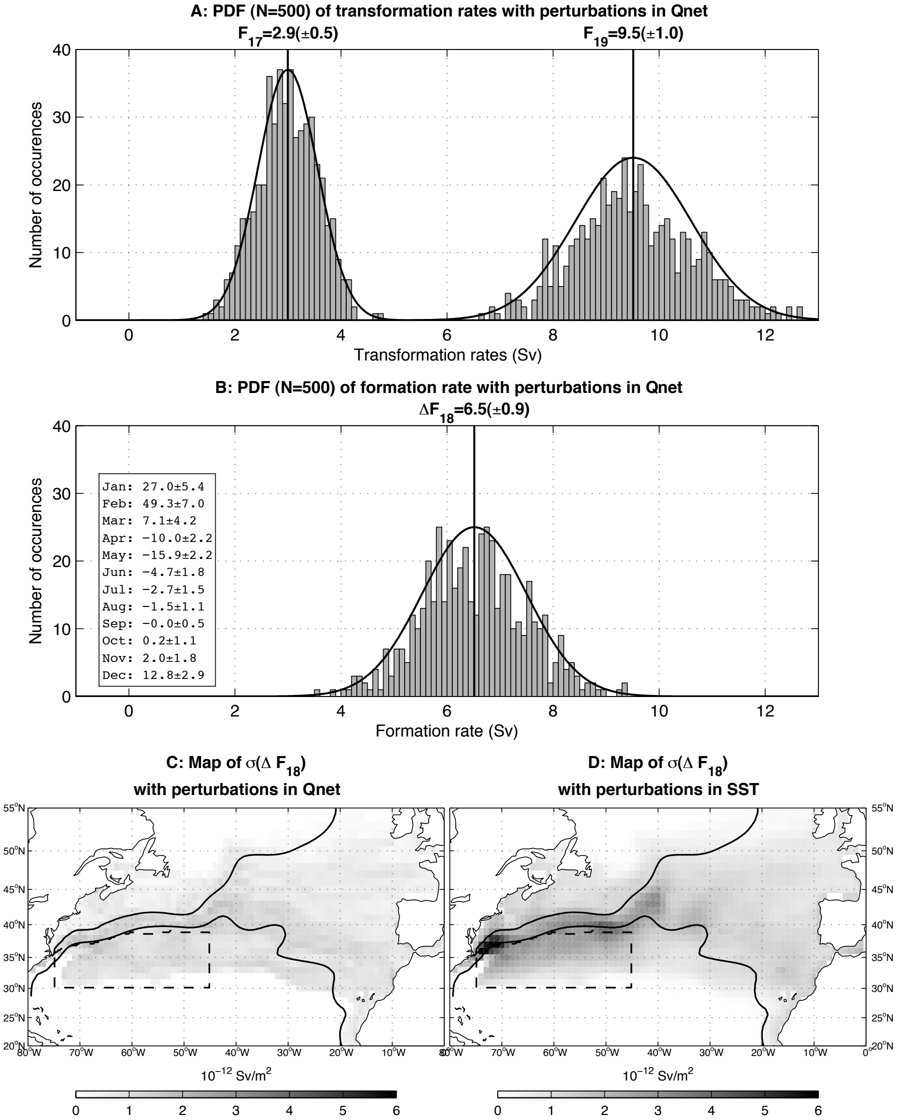

Figure 9: From the OCCA dataset: PDFs of transformation $F(17^oC)$, $F(19^oC)$ (panel A) and formation $\Delta F(18^oC)$ (panel B) rates for the first ensemble experiment where only the air-sea heat flux is perturbed (see text). In Panel B, monthly mean and standard deviation of $\Delta F(18^oC)$ are tabulated. Lower panels: maps of local standard deviation of $\Delta F(18^oC)$ for the first (panel C) and second (panel D) ensemble with perturbations on Q_{net} and SST only respectively. Dashed black line is the formation box area and two thick black contours are mean $-0.2m$ and $-0.6m$ SSH from OCCA.

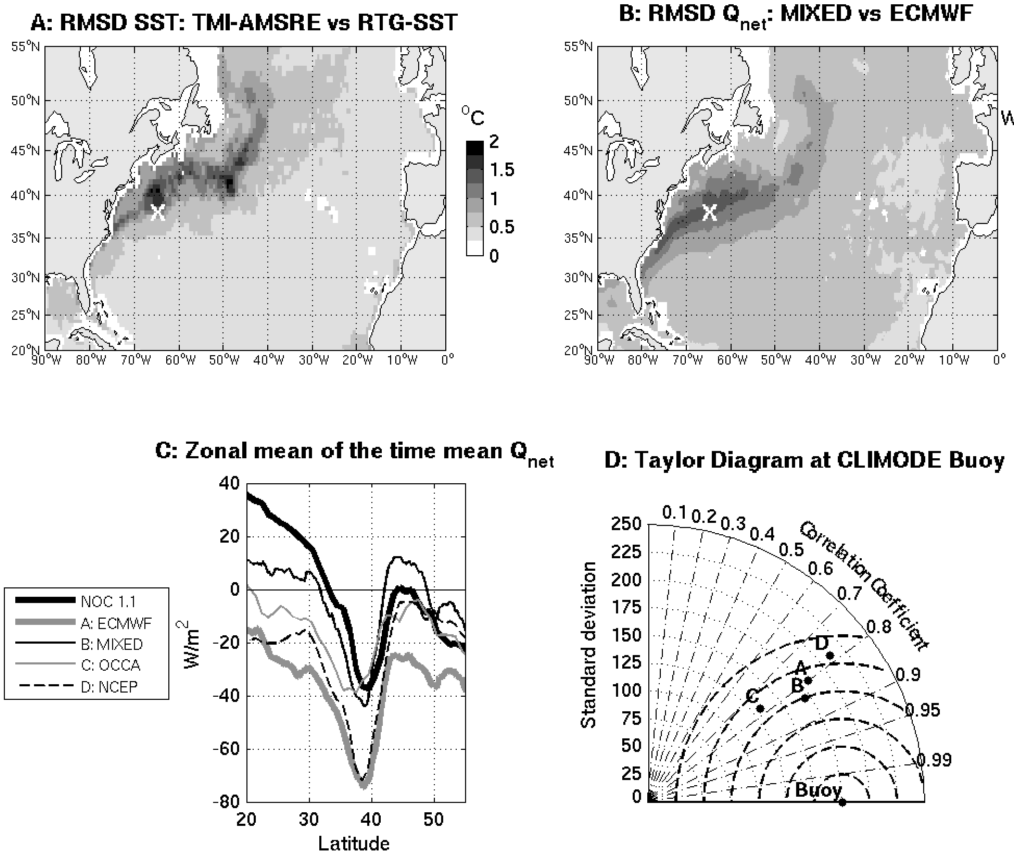

Figure 10: Panel A: RMS difference between daily TMI-AMSRE and RTG SSTs from 2004 to 2006. Panel B: RMS difference between daily MIXED and ECMWF Analysis sea-surface heat fluxes from 2004 to 2006. Panel C: Zonal mean of sea-surface net heat fluxes time mean from the National Oceanographic Center Version 1.1 (from 1991 to 2005, monthly fields), ECMWF Analysis (2004-2006, daily fields), MIXED (2004-2006, daily fields), OCCA (2004-2006, daily fields) and NCEP-R1 (2004-2006, daily fields). Panel D: Taylor diagram from local daily sea-surface net heat fluxes at the CLIMODE mooring localized at 38.5N/65W and denoted as the white cross in panels A and B. Individual points A, B, C and D stand for ECMWF, MIXED, OCCA and NCEP datasets respectively.

List of Tables

Grid Resolution	Temperature class bin: $\Delta\theta$			
	1	1/2	1/4	1/8
1^o	**5.76** (12.8;-7.07)	**6.38** (14.2;-7.85)	**6.47** (15.2;-8.77)	**7.48** (17;-9.53)
$1/2^o$	**5.1** (12.1;-6.96)	**5.73** (13.5;-7.79)	**5.62** (14.3;-8.71)	**5.94** (15.6;-9.68)
$1/4^o$	**5.27** (12.1;-6.83)	**5.65** (13.4;-7.74)	**5.8** (14.4;-8.57)	**5.81** (15.7;-9.91)
$1/8^o$	**5.25** (12.1;-6.86)	**5.69** (13.4;-7.7)	**5.87** (14.4;-8.51)	**5.88** (15.7;-9.8)

Table 1: 2005 Mean formation rates $\Delta F(18^oC)$ from the OCCA dataset for various temperature class bin and horizontal grid resolutions. Values in parenthesis are domain integrals over positive and negative areas only.